

Observations of Tidal Melt and Vertical Strain at the Filchner-Ronne Ice Shelf, Antarctica

Irena Vaňková¹, Keith W. Nicholls¹, Hugh F. J. Corr¹, Keith Makinson¹, and Paul V. Brennan²

¹British Antarctic Survey, Natural Environment Research Council, Cambridge, UK, ²Department of Electronic and Electrical Engineering, University College London, London, UK

Key Points:

- Estimates of tidal melt at the base of an ice shelf are derived from phase-sensitive radar measurements
- Observations of basal melt at tidal frequencies may help constrain sub-ice shelf ocean flow regime
- M_2 tidal vertical strain is depth uniform at most sites, but at four sites local effects cause tidal bending to dominate

Supporting Information:

- Supporting Information S1

Correspondence to:

I. Vaňková,
irkova@bas.ac.uk

Citation:

Vankova, I., Nicholls, K. W., Corr, H. F. J., Makinson, K., & Brennan, P. (2020). Observations of tidal melt and vertical strain at the Filchner-Ronne Ice Shelf, Antarctica. *Journal of Geophysical Research: Earth Surface*, 126, e2019JF005280. <https://doi.org/10.1029/2019JF005280>

Received 26 JUL 2019

Accepted 24 DEC 2019

Accepted article online 5 JAN 2020

Abstract The Filchner-Ronne Ice Shelf experiences strong tidal forcing known to displace portions of the ice shelf by several meters over a tidal cycle. These large periodic displacements may cause significant variation of the ice shelf vertical strain. Further, tidal currents in the ice shelf cavity may be responsible for basal melt variations. We deployed autonomous phase-sensitive radio-echo sounders at 17 locations across the ice shelf and measured basal motion and internal vertical ice motion at sufficiently short intervals to allow the resolution of all significant tidal constituents. Basal melt estimates with this surface-based technique rely on accurate estimation of vertical strain changes in the ice shelf. We present a method that can separate the vertical strain changes from the total thickness changes at tidal time scales, yielding a tidal basal melt estimate. The method was used to identify vertical strain and basal melt variations at the predominant semidiurnal M_2 tidal constituent. At most sites the tidal vertical strain was depth independent. Tidal deformation at four sites was controlled by local effects causing elastic bending. Significant tidal melt was observed to occur at six locations, and upper bounds on the tidal melt amplitude were derived for the remaining sites. Finally, we show that observations of basal melt spectra, specifically at tidal frequencies and their multiples, can provide constraints on the hydrographic conditions near the ice base, such as the nontidal background ocean flow.

1. Introduction

Ice shelves are an integral part of the Antarctic Ice Sheet, and as they float in the surrounding ocean, they provide a pathway for oceanic changes to influence the inland ice sheet. Ocean tides play a potentially important role in the overall dynamics of the ice shelf/ocean system (Padman et al., 2018). These dynamics are particularly pronounced for the Filchner-Ronne Ice Shelf (FRIS). Floating in the Weddell Sea, FRIS experiences strong tidal forcing known to displace portions of the ice shelf by several meters over a tidal cycle (Doake, 1992). Such large displacements significantly affect ice shelf flow. GPS-derived measurements of FRIS surface velocities have shown that their tidal components can be larger than the mean flow speed by a factor of up to three (Makinson et al., 2012).

The effect of tides on the hydrographic conditions beneath the ice shelf is also substantial. Strong tidal currents have been observed in the FRIS cavity (Nicholls et al., 1997) and also modeled (e.g., Makinson & Nicholls, 1999; Mueller et al. (2018). Makinson et al. (2011) used a model to show that as tides energize the flow in the ice shelf cavity, the basal melt/freeze spatial pattern is enhanced, highlighting the important role ocean tides play in setting the mean basal melt rates for FRIS. Several modeling and theoretical studies investigated the role that tides may play in the mechanisms by which heat is brought near to the ice shelf base and made available for melting (e.g., Scheduikat and Olbers (1990), Makinson (2002), Gwyther et al. (2016)). Some mechanisms imply melt rate variability over the tidal cycle. Because the strongest tidal forcing in the Weddell Sea comes from the semidiurnal tidal band, detecting the corresponding melt rate variability would require frequent sampling and a high precision technique capable of detecting small changes at the ice shelf base.

To observe this level of detail in the melt rate variability, local measurements are required. Grosfeld et al. (1994) collected data through a borehole and showed a tidal variation in the temperature near the ice base; however, their measurements of melt rate gave a mean over a 2-year period. The approach to observing ice shelf basal melt changed with the development of a ground-based phase-sensitive radar (Corr et al., 2002). This technique detects changes in vertical positions of internal and basal ice reflectors between repeated

measurements, which can be used to derive a melt rate. Frequent repetition of these measurements can reveal variability in the ice shelf dynamics, the basal melt rate, or both. Jenkins et al. (2006) applied this technique near the FRIS grounding line and found that the derived mean melt rates were at the lower end of prior estimates. They also observed tidal variations in the internal ice reflectors and found evidence of elastic ice shelf bending over the tidal cycle. They did not, however, observe any notable melt rate variability.

A dramatic improvement in the practicality of this observational technique came with the development of the autonomous phase-sensitive radio-echo sounder, ApRES (Brennan et al., 2014; Nicholls et al., 2015). This robust and low-power instrument is now capable of autonomously collecting repeated observations over an entire season at temporal resolutions that allow the detection of variability at tidal frequencies. ApRES observations are now beginning to be used to derive seasonal to weekly basal melt rate variations (Stewart, 2018; Davis et al., 2018). The main challenge with deriving melt rates with a phase-sensitive radar lies in accurate estimation of the vertical strain rate profile. While the basal reflector is usually strong, internal ice reflectors are relatively weak, yet it is the relative motion of these internal ice reflectors that is used to determine the ice dynamical contribution to the total ice thickness change. Consequently, uncertainties in the vertical strain are a primary source of uncertainty in the basal melt rate. As the time scale of interest becomes shorter, these uncertainties increase. Therefore, separating vertical strain rate and basal melt rate on semidiurnal tidal time scales can be challenging.

In this paper, we push the limits of the ApRES observational technique to detect ice shelf vertical strain and basal melt down to semidiurnal tidal time scales—the fastest time scales that can be resolved with the 1- to 2-hourly sampling interval of typical year-round Antarctic deployments. We use data collected at 17 FRIS sites between years 2015 and 2017 and then develop a method for the separation of melt and vertical strain at tidal time scales. The paper is structured as follows. The data sets used are described in section 2. The method for separating tidal strain and melt thinning is presented in section 3. For clarity, this section also provides necessary background on data processing and methods developed in the past that we rely on. Strain and melt results from individual sites are analyzed in section 4. In section 5 we discuss mechanisms that could cause the observed tidal melt and illustrate the potential use of tidal melt measurements in constraining background ocean flow regimes near the ice shelf base. We summarize our conclusions in section 6.

2. Data

2.1. ApRES Observations

Seventeen ApRES instruments were deployed on the surface of FRIS during years 2015–2017. A map showing the deployment sites is given in Figure 1a. Operational periods with good quality data for each instrument are summarized in Figure 1b. Battery problems caused several instruments to stop working after approximately 6 months. Additionally, instruments at some sites experienced time periods during which the prescribed attenuator settings were not correctly loaded; these time periods, characterized by frequent abrupt jumps, were excluded from further analysis. The ApRES sampling time interval was set to 1 hr at Site5c and to 2 hr at all other sites, allowing for resolution of the tidal frequencies known to dominate in this region.

2.2. Tidal Model Output

We obtain information about the tidal ice shelf elevation changes and tidal currents using output from the CATS2008 regional tidal model, an update to the model described by Padman et al. (2002). This output is used in section 5 to estimate the ocean background flow beneath the ice shelf. According to the model output, the largest amplitude tidal constituent at all 17 ApRES sites is M_2 (see Figure 2a), and we use this constituent to illustrate the applicability of the methods presented here.

3. Methods

3.1. Processing

The main steps of the ApRES signal processing are summarized here; for full details the reader is referred to Brennan et al. (2014) and Nicholls et al. (2015).

At the beginning of each 1- or 2-hr time interval the instrument transmits a burst, consisting of a sequence of, typically, 30 chirps. Here, a chirp is a signal whose frequency ramps from 200 to 400 MHz over a period of 1 s. The received signal level is carefully controlled using appropriate levels of amplification and attenuation to ensure the resulting signal remains well within the limit of 0–2.5 V before it is digitized. Postprocessing

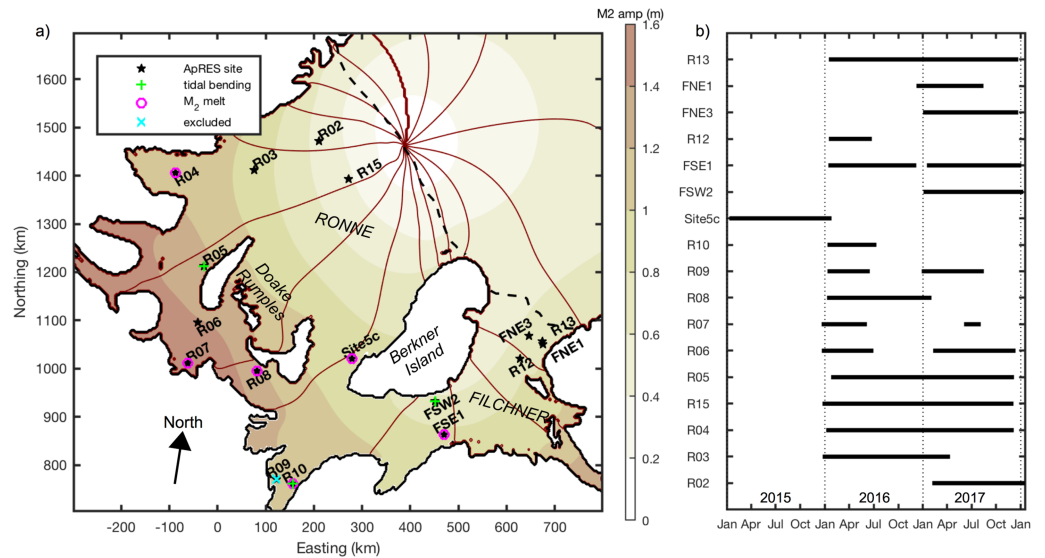


Figure 1. (a) M_2 tidal constituent over the Filchner-Ronne Ice Shelf from the CATS2008 tidal model (Padman et al., 2002). M_2 amplitude is shown as filled contours in the background; lines of constant M_2 phase spaced by 22.5° are in red. Approximate location of ice shelf front is marked with black dashed line. Tidally bending sites and sites where M_2 tidal melt was significant are highlighted. (b) Period of ApRES operation for each site.

is centered on spectral analysis, because each frequency contained in a received chirp is related to a unique range between reflector and antenna. To increase the signal-to-noise ratio, we use a burst-averaged chirp in the postprocessing. The final product is a depth profile of complex numbers containing information about the amplitude and phase of the received signal at each time step.

A small portion of the preprocessed signal clipped (as a result of exceeding the 0- to 2.5-V limit during digitization) at site R06. To ensure no clipping-related artifacts are present, at this site we postprocessed

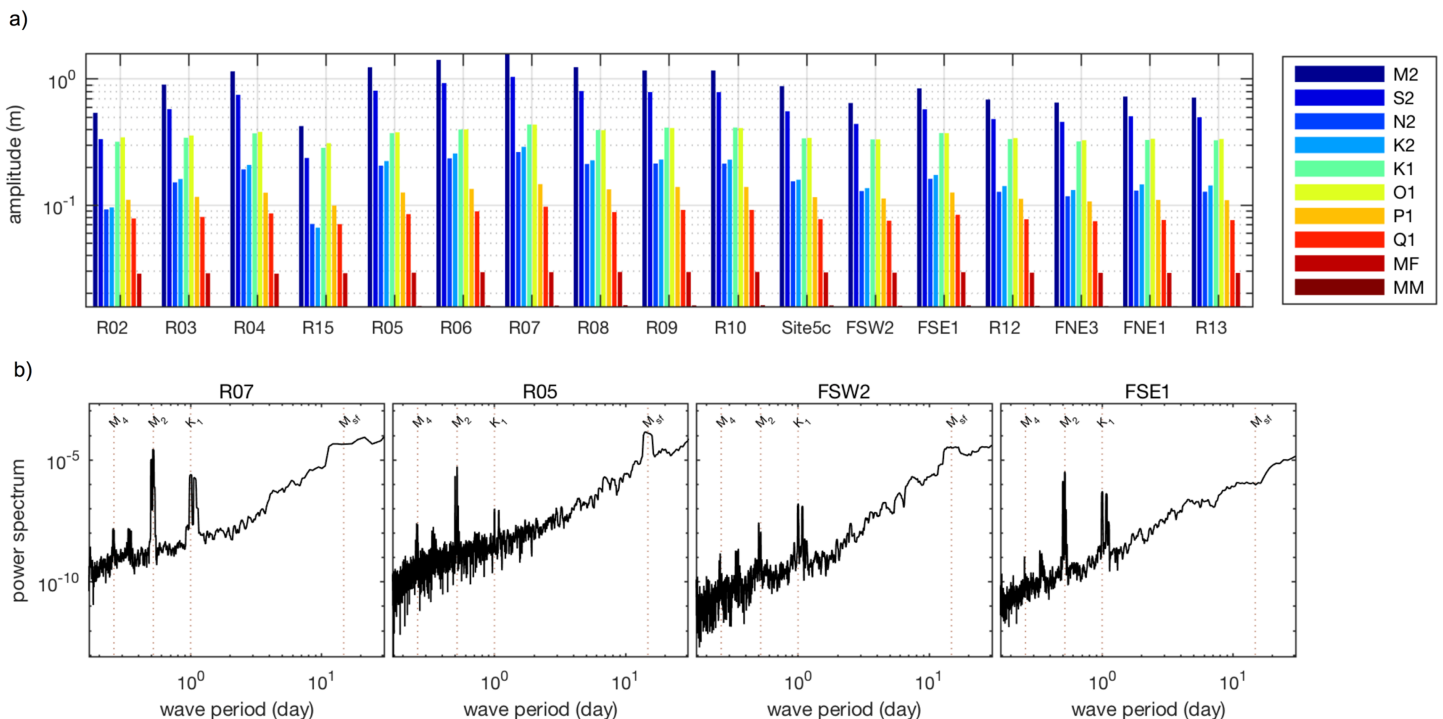


Figure 2. (a) Amplitude of different tidal constituents at each deployment site extracted from a tidal model. (b) Power spectrum of the basal reflector time series at four example sites.

only a subinterval of each burst-averaged chirp to avoid the clipped signal portion. The only consequence of doing this, as opposed to using the full received chirp, is a lower vertical resolution in the amplitude profile because of its bandwidth dependence and a slightly reduced signal-to-noise ratio. For all other sites the entire 1-s burst-averaged chirp was postprocessed.

3.2. Time Series

The temporal sequence of depth profiles created by the steps outlined in section 3.1 is now used to construct time series of vertical displacement of individual ice reflectors with respect to the instrument placed at the ice shelf surface. Henceforth, displacement, velocity, and strain are assumed to refer to the vertical direction; further, as they are referenced to the antennas, the displacements are depth cumulative unless otherwise specified. The displacement time series will be used later to understand the dynamics of the ice column, a requirement for deriving a basal melt estimate.

One way to create displacement time series is simply to find the phase difference between each pair of consecutive time shots at each depth level and convert it to distance (e.g., following Vaňková et al. (2018)). One disadvantage of this approach is that it treats weak and strong reflectors equally and, as a result, some time series may show unrealistic behavior, presumably caused by noise dominating weaker signals. These time series then need to be excluded at a later time using statistical tools.

Here we use an alternative method to construct displacement time series, which is based on cross correlation of portions of the series of postprocessed chirps (Nicholls et al., 2015; Stewart, 2018; Stewart et al., 2019). The method was originally developed by Stewart (2018) to analyze infrequent ApRES observations, typically collected 1 year apart. It is not uncommon that, over such a long time interval, the ice deforms sufficiently to make the phase-differencing approach inapplicable. An additional advantage of the cross-correlation approach is that it has an inherent degree of vertical averaging and weights the result according to the signal strength.

First, the return signal depth profile is divided into segments of prescribed length (typically 4–8 m, here 4 m). For a pair of profiles, return signal segments corresponding to a given depth range are cross-correlated. The cross-correlation lag between the two return signal segments gives the displacement of a given depth layer over the sampling interval. This is repeated for each pair of time-consecutive samples and for all depth segments. A displacement time series for a given depth level is then produced by cumulatively adding the individual displacements. Additionally, a normalized correlation coefficient is computed for each depth and each time interval, providing an indication of the reliability of the time series. The correlation coefficient is a measure of similarity between the lagged signals, while a strong reflector is likely to produce a return signal whose waveform remains relatively intact over time, giving a high coefficient, a weak reflector will have its waveform distorted by noise (due to low signal-to-noise ratio), resulting in a lower coefficient. With a 2-hr sampling interval the correlation coefficient is generally very close to 1 at all depths, and thus, small changes in its value may indicate substantially weaker internal reflectors.

In addition to these two methods, if there is a distinct strong and persistent reflector present in the return signal, displacement time series can be created by tracking this strong reflector directly. For an ice shelf, the basal reflector at the ice ocean interface is generally well suited to this method. First, the basal reflector, an abrupt and persistent increase in the return amplitude (e.g., Corr et al., 2002), is identified in the first sample. The local maximum of this basal return is tracked through time as its distance from the surface evolves. To avoid abrupt jumps in this time series, which could occur as a result of slight changes in the shape of this basal return if the time series was given simply by the range from the surface of the amplitude peak, we use the phase information to calculate the position of this reflector. Because the phase of nearby reflectors at the base is close, small changes in the shape of the basal peak return amplitude and the associated local maximum have little effect on the result. To get a displacement time series of the basal reflector, this approach is preferred to cross correlation because it avoids problems when the basal reflector moves from one depth segment to another.

The displacement time series of the basal reflector X_{total} gives the evolution of the total ice thickness, which includes contributions from ice dynamics, basal melt, and surface and near-surface effects (Corr et al., 2002):

$$X_{total} = X_{strain} + X_{melt} + X_{surf}, \quad (1)$$

where X_{strain} is thinning due to vertical straining, X_{melt} is thinning due to melting, and the last term X_{surf} combines thickness changes due to surface and near-surface processes including firn compaction, sinking of the instrument, and apparent surface changes related to the instrument's sensitivity to temperature. The X_{strain} and X_{surf} terms need to be determined from the internal reflector time series, and X_{melt} is computed from equation (1). The method for identifying X_{strain} and X_{surf} contributions may vary based on the time scale of interest.

3.3. Long-Term Mean

Nicholls et al. (2015) derived the long-term means of X_{strain} and X_{surf} using the first and last sample. Here, we use the full data set. First, we find the displacement that an internal reflector would accrue if the velocity with which it moves with respect to the antennas was constant over a given time period. The mean velocity is given by the slope of the line of best fit to the displacement time series. These displacements are then plotted as a function of depth, and a long-term vertical displacement profile can be estimated by fitting an appropriate curve to these data. The curve fit is weighted by the inverse error found from using the linear fits to the time series. The vertical strain, ϵ_v , is given by the vertical derivative of this curve.

For a freely floating ice shelf ϵ_v is expected to be depth independent, in which case all internal layers of the same thickness vertically thin or thicken by the same amount, depending on whether the ice is in a horizontally extensive or compressive regime. Because the vertical displacements are depth cumulative, the curve to be fitted is a straight line. However, features in the ice shelf topography (e.g., basal channels), proximity to grounding lines, or spatial variability in ice shelf properties on short horizontal spatial scales may cause the ice shelf to be in a state of adjustment toward flotation, causing ϵ_v to be a function of depth because of the presence of vertical shear stresses; this has been observed (Jenkins et al., 2006) and also modeled (Vaughan et al., 2012). In these cases there is a region of relative compression in one part of the ice column separated by a neutral surface from a region of relative extension in the other part. The simplest case of depth-dependent ϵ_v is when the shear stress is constant with depth. Then ϵ_v is a linear function of depth, and the curve to be fitted to the depth-cumulative displacements is a quadratic function. Jenkins et al. (2006) found that this model was appropriate to explain observations at several sites near the FRIS grounding line by Rutford Ice Stream. The shear stress and ϵ_v may be a more complicated function of depth, depending on a number of local factors. Identification and justification of a more complicated functional fit may require complementary observations.

To estimate the mean melt $\overline{X_{melt}}$ from equation (1), the remaining three terms are derived as follows. $\overline{X_{strain}}$ is given by the difference between the basal and surface intercepts of the curve fitted to the depth-cumulative vertical displacements, $\overline{X_{surf}}$ is the surface intercept of the fitted curve, and $\overline{X_{total}}$ is the mean displacement of the basal reflector. Because ApRES measures displacements and not velocities, the analysis is often best carried out directly on the displacement time series, yielding melt (in units of length) rather than melt rate. However, for the long-term mean, melt rate can be easily obtained in the same way as above if mean vertical displacement is substituted by mean vertical velocity and its depth profile fitted with a curve whose derivative is the vertical strain rate.

3.4. Tides

The above approach can in principle be used for any time interval; however, as the interval becomes shorter, the fit used to determine $\overline{X_{strain}}$ and $\overline{X_{surf}}$ becomes less well constrained, primarily because the internal reflectors are weak and the reflector motion over a short time interval is small. However, for fluctuations at tidal frequencies, which are known exactly, an approach based on tidal analysis is possible.

For each site we first apply tidal analysis to the detrended internal and basal reflector time series. To extract tidal constituents, we use the UTide package (Codiga, 2011), which utilizes a robust iteratively reweighted least squares regression fit to the tidal frequencies. This returns the tidal amplitude and phase of the vertical displacement of reflectors for the tidal constituents that the time series is long enough to resolve. The changes in a tidal constituent's amplitude and phase with depth allow us to study the nature of elastic deformation processes acting within the ice shelf, in the same way as the long-term motion allows the study of viscous deformation. In the case of depth-uniform tidal compression/extension, the tidal amplitude increases linearly with depth, and the tidal phase is constant. In the case of tidal bending around a neutral surface, the tidal amplitude fits a quadratic profile, and the tidal phase is constant until about twice the neutral surface depth and then reverses by 180°. The factor of 2 enters because it takes sufficient distance for a

reversal of phase to appear in a depth-cumulative time series. Again, knowledge of the tidal behavior of the ice is crucial for determining tidal-band melt thinning fluctuations, ξ_m .

ξ_m can be found from equation (1), where X_{strain} is defined by ξ_s , the tidal-band cumulative strain thinning fluctuations at the basal intercept determined from the curve fit, and X_{total} is given by ξ_t , the total tidal-band thinning fluctuations given by the tidal displacement of the basal reflector. However, rather than constructing time series, subtracting and detiding them, in this case it is easier to calculate the ξ_m phasor (vector describing the ξ_m amplitude and phase) by differencing the ξ_t and ξ_s phasors. If the tidal oscillation of the basal and internal reflectors happen to be exactly in-phase, the ξ_m phase is also the same, and the ξ_m amplitude is simply given by the difference between the ξ_t and ξ_s amplitudes. However, there is no reason to expect the tidal signals in the displacements of the basal and internal reflectors should be in phase, because tidal fluctuations in melt and strain are caused by different physical mechanisms. Small differences in the phase of ξ_t and ξ_s phasors can result in a large change of the phase of the estimated ξ_m phasor. Note that the uncertainty in ξ_s amplitude/phase can introduce uncertainty in either or both amplitude and phase of ξ_m .

At the M_2 tidal frequency, which we focus on here, we expect $X_{surf} = 0$, because we are not aware of processes independent of the tidal strain that would act to introduce the M_2 tidal constituent into the surface processes. This is not the case for all tidal constituents; for example, K_1 , which has a period very close to 24 hr, may be contaminated by a diurnal temperature signal due either to temperature-induced changes in the dielectric properties of the upper snow surface or, more likely, to an instrumental response to temperature changes. Such an effect would result in a nonzero surface intercept in the tidal amplitude versus depth plot. For M_2 , considered here, the curve fitted to the tidal amplitude depth profile could be constrained to pass through zero at the surface. We do not do this, however, as the size of the surface intercept helps indicate the suitability of the linear or quadratic model. Consequently, the surface intercept of the tidal amplitude curve fit is treated here as an additional source of uncertainty on the ξ_m estimate.

To make ξ_s and, therefore, ξ_m estimates more robust, we divide each time series into a number of shorter intervals for tidal analysis. This reduces the number of constituents that can be extracted and, while it does not affect the M_2 constituent we focus on here, the length of the intervals might need increasing for analysis of different tidal constituents. Here we used 60-day intervals with a 20-day overlap. The mean tidal amplitude and phase of each time series are then used to find the appropriate fit to the depth profile, weighted by the inverse of the respective errors determined from the tidal analysis. There are a number of factors that can cause certain internal reflectors to be unsuitable for the curve fit, although no objective way of evaluating suitability has been developed yet. Correlation coefficient is generally a good indicator of the quality of internal reflectors; however, a potential problem is that strong off-nadir reflectors, such as buried crevasses, will also give high correlation coefficient. Time series generated by off-nadir reflectors should not be included in the extrapolation of the vertical strain profile because their perceived vertical displacement over time has a horizontal motion component. Here the depth interval over which the curve fit is made is chosen manually, with the choice being guided by (1) the scatter of the tidal phase/amplitude estimate and (2) the phase/amplitude correlation coefficient determined from cross correlation. High scatter in the tidal phase/amplitude estimate and a drop in the correlation coefficient are typically reasons for excluding certain depth intervals from the fit. To account for the error resulting from the sensitivity to the choice of fitting points, we use the following bootstrapping approach. We generate random subsets from the set of points that are left after the removal of unsuitable depth intervals, and we fit a curve to each of these subsets. This is repeated 1,000 times for different subsets consisting of 60% of the eligible points, where each subset is drawn from a uniform distribution without repetitions. This provides a means of estimating the uncertainty in the resulting ξ_s , which is generally larger than the standard error from each of the curve fits. The confidence interval for the ξ_s estimate is based on the middle 90% of fits.

The final ξ_m amplitude uncertainty is a combination of the ξ_s and ξ_t amplitude and phase uncertainties, which include the errors in the estimation of tidal constituents of the internal and basal reflectors, and the error indicated by a nonzero surface intercept.

4. Results

At each of the 17 sites we have constructed time series of vertical displacements of internal reflectors and the basal reflector. The power spectrum of the basal reflector time series is shown in Figure 2b for four example

sites. At all sites there are strong tidal peaks, primarily in the semidiurnal and diurnal frequencies; however, quarterdiurnal and terdiurnal tides also appear. At some sites the fortnightly M_{sf} constituent is present and strong while at others it is completely absent. The strongest and cleanest signal in the internal reflectors is that of the semidiurnal M_2 constituent. For FRIS, ice shelf tilt has been shown to explain semidiurnal tidal variations in ice shelf flow (Makinson et al., 2012; Rosier & Gudmundsson, 2019). M_2 being the strongest signal in the internal reflectors is therefore consistent with M_2 having the largest amplitude in the ocean tidal model (Figure 2a). To identify a melt contribution to the basal reflector time series at a particular time scale, we need a good estimate of the vertical strain contribution. Therefore, to illustrate the applicability of the method, we focus here on separating melt and vertical strain at the M_2 frequency.

After extracting the M_2 phase and amplitude at each depth, we analyze the resulting depth profiles to decide which vertical strain model best fits the observations. The two models we consider are constant vertical strain (linear fit to displacements), and vertical strain depending linearly on depth (quadratic fit to displacements). The sites where neither of these two models is appropriate are not analyzed further. Jenkins et al. (2006) used the statistical F test to discriminate between quadratic and linear fits in the long-term mean, and we use that technique here for both long-term mean and tides, together with physical arguments, to discuss which model is more appropriate at each site. Finally, after ξ_s has been determined, we calculate ξ_m .

4.1. Sites With Depth-Uniform Tidal Vertical Strain

The tidal amplitudes of the internal layers at sites R02, R03, R04, R06, R07, R08, R12, R15, Site5c, FNE3, FSE1, and FNE1 are well fitted by a straight line, implying a tidal vertical strain that is constant with depth (example of site R07 in Figure 3, and the remaining sites in Figure S2 in the supporting information). There are a few sites where the F test would suggest that a quadratic fit is statistically better, but where physical constraints indicate that this is not appropriate. For sites FSE1, R03, FNE1, and R08 the quadratic fit produces a neutral surface that lies outside the ice column, which is unrealistic. Additionally, the difference between ξ_s derived from either fit at these four sites is small; therefore, the choice of a fit has little effect on the ξ_m estimate. At site FNE3 the linear fit has a much smaller surface intercept than the quadratic fit; also, the quadratic fit here, although statistically slightly better, is highly sensitive to the points included in the fit. As a result, we argue that the simpler linear fit at FNE3 is sufficient. However, the tidal phase in the upper part of the ice column is poorly constrained, hiding a possible phase reversal in case of bending over the suggested neutral surface. Overall, at FNE3 the choice of a fit has little effect on the ξ_s amplitude estimate. At Site5c the F test suggests a quadratic fit is better; however, we do not observe a reversal of tidal phase with depth, which the location of the neutral surface at ~ 80 -m depth would suggest should be at ~ 160 m given that the internal reflector time series are depth cumulative. At Site5c the phase signal is robust, unlike at FNE3, showing constant phase throughout the ice column, which supports depth-independent tidal strain. For all these 12 sites, long-term mean vertical strain rate is also depth independent (shown in Figure S1). This is consistent with the locations of these sites, on open ice shelf, away from grounding lines.

4.2. Sites With Depth-Variable Tidal Vertical Strain

FSW2, R10, and R05 (examples of FSW2 and R05 in Figure 3 and R10 in Figure S2) are sites where a straight-line fit to the depth-cumulative tidal amplitudes of the internal reflector vertical motion does not suffice. Here we discuss these sites one by one and provide physical or statistical arguments why a quadratic fit, implying that tidal vertical strain is a linear function of depth, is a better model.

The most straightforward of these sites is R05, where an application of the F test shows that a quadratic model gives an improved fit over the linear alternative. At this site we further observe a change in tidal phase with depth by $\sim 180^\circ$, consistent with tidal bending. Using the quadratic fit, we find that the neutral surface at R05 is located at ~ 200 m. Consistent with that, the tidal phase change occurs at a depth of ~ 400 m.

FSW2 and R10 have similar characteristics. Although in neither case does the F test show that a quadratic fit is statistically better than a linear one, the quadratic fit appears more suitable. At both sites the linear fit produces large surface intercepts, implying large apparent tidal displacements in the near-surface layers, while for a quadratic fit the surface intercepts are small. Further, for the quadratic fit there is a lower sensitivity to the choice of a subset of suitable points over the fitting region. Unlike for site R05, the phase information does not help discriminate between the fits. The ~ 860 -m-thick site FSW2 has a neutral surface at ~ 480 -m depth, approximately half way through the ice column. R10 is $\sim 1,340$ m thick, and its neutral surface is located at $\sim 1,100$ m, which is in the bottom fifth of the ice column. Because the neutral surface is at

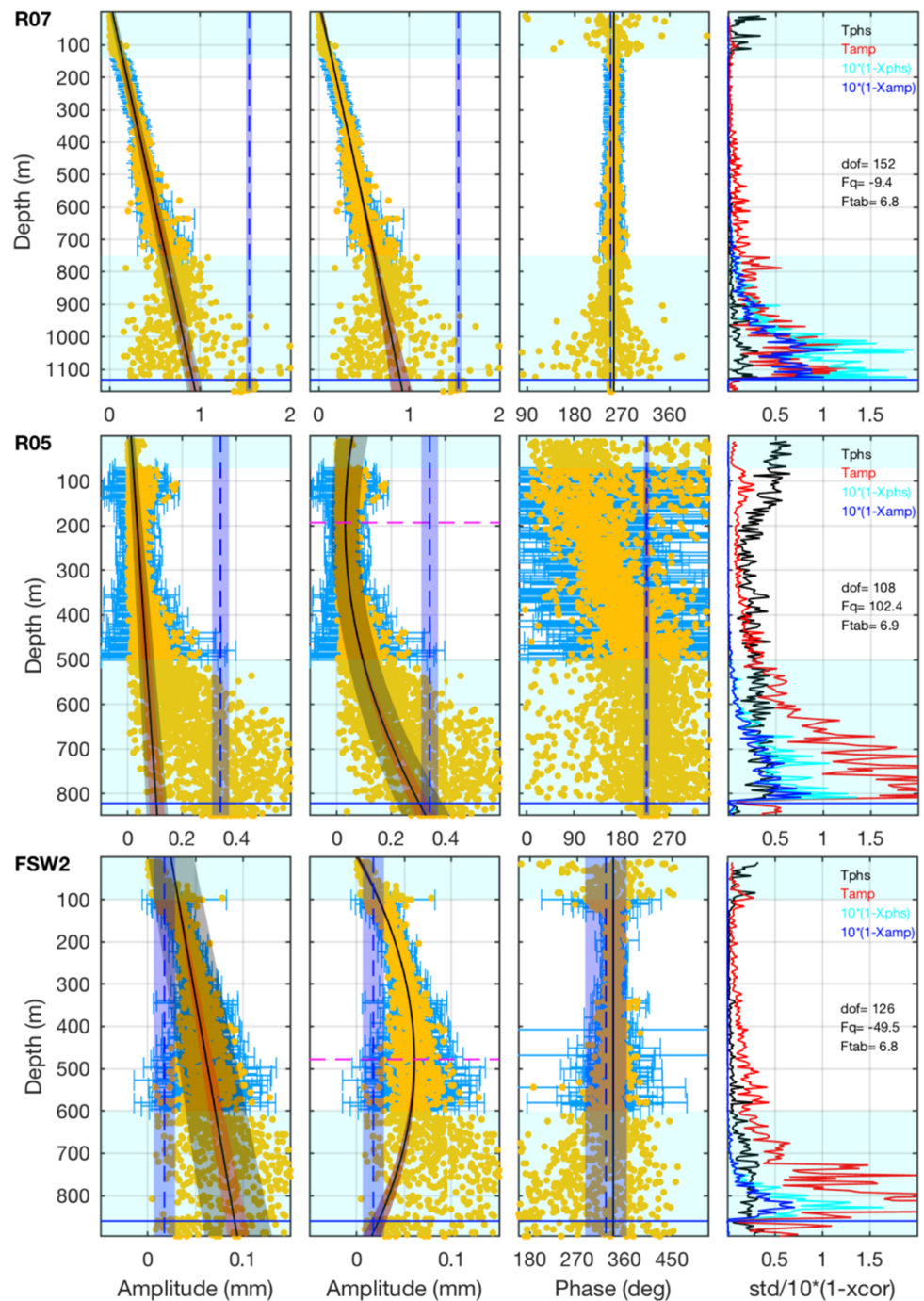


Figure 3. Results for M_2 tidal frequency in the internal and basal reflectors at three example sites. (First column) The yellow dots show tidal amplitude of internal reflectors from UTide; error bars in blue are included for those depths that were used for fitting. The black line is the mean of the straight line fits, the red shading contains 90% of the slopes generated by bootstrapping, and the gray shading highlights the error due to surface intercept. The solid blue line indicates bed location. The dashed blue line is the tidal amplitude of the basal reflector with shading showing the standard error. (Second column) Same as the first column but for a quadratic fit. When available, the neutral surface is shown with dashed magenta line. (Third column) Same as the first column but for tidal phase. (Fourth column) Indicators of the quality of internal reflectors: normalized standard deviation of tidal phase (black, Tphs) and tidal amplitude (red, Tamp), and 1-mean correlation coefficient (scaled by factor of 10 for better visibility) as derived from the time series construction for phase correlation (cyan, 1-Xphs) and amplitude correlation (blue, 1-Xamp). The cyan-shaded regions are excluded from curve fitting. F test values are printed in black, when F_q is larger than F_{tab} , quadratic fit is statistically more significant than the linear fit.

mid-depth or deeper at these two sites, and because the internal reflector time series are depth cumulative, reversal of the tidal phase does not occur.

Because FSW2, R10, and R05 are located near the ice shelf grounding line, tidal bending effects are expected at these sites, providing an additional physical justification for quadratic fits. However, all three sites appear to be in hydrostatic equilibrium over the long-term mean: There is no indication of depth dependence of the mean vertical strain rate (Figure S1).

4.3. Other Sites

R13 is a more complicated site than the above. The F test favors a quadratic model, although a quadratic fit suggests a shallow neutral surface, at 80-m depth in an ice column ~ 600 m thick. There is a large spread in the tidal phase estimate between different time segments, but in the top 160 m this is even larger. It is possible that this spread in tidal phase obscures a phase reversal, and the fact that one is not observed does not automatically imply that the tidal vertical strain is depth uniform. At R13 the long-term mean is also better fitted with a quadratic, rather than a linear profile, not only statistically (again using F test) but also physically (Figure S1); further, the long-term neutral surface coincides with the tidal neutral surface. In the long-term mean a linear fit would imply expansion rather than compaction in the firn layer, while a quadratic fit is consistent with firn densification. While R13 is located far from the nearest grounding line, there is a rift nearby, which may have the effect similar to that of a large subglacial channel. The shallow position of the neutral surface is consistent with the location of sea ice in the rift, which would further justify why the quadratic fit better describes both the long-term mean vertical displacement and the tidal amplitude of the internal reflectors. As seen later in section 4.5 for R13 the choice of a linear versus quadratic model has profound consequences for the long-term mean melt rate estimate: With a linear model the melt rate would be nearly 1 m/year while with a quadratic fit the melt rate is small and its sign uncertain. In section 4.5 we include results from both linear and quadratic fits for R13. The linear fit can be thought of as the upper bound and the quadratic fit as the lower bound for the mean melt rate at R13.

Site R09 has a complex vertical structure both in the long-term mean and on tidal time scales. First, investigation of the tidal phase shows that a reversal by 180° occurs twice, first at ~ 70 -m depth and then again at ~ 300 -m depth. This indicates that neither of the two vertical strain models is appropriate at this site. Below ~ 550 m, the scatter in the phase estimates from different time segments quickly increases, indicating poor internal reflectors, consistent with the rapidly decreasing correlation coefficient. The cumulative tidal amplitude increases at different rates, first slowly down to ~ 300 -m depth, and then there is a sudden abrupt increase between 300 and 400 m, and the amplitude increase again down to ~ 550 m, below which the estimate becomes unreliable. The vertical profile of the ice motion in the upper half of the ice column at site R09 is sufficiently complicated that extrapolation beneath ~ 550 m is unjustified without some additional knowledge about the local ice behavior. The long-term mean vertical displacement profile is also complicated, suggesting several regions of compression and extension. At present, the constraints on the basal contribution due to strain are insufficient to provide a reliable estimate of either the long-term mean melt or ξ_m , and we do not discuss R09 any further.

4.4. Tidal Melt Estimate

Here we use the tidal amplitude and phase of the basal reflector and of the cumulative strain thinning at the ice shelf base to compute ξ_m . As explained in section 3.4, this is done by subtracting the ξ_s phasor from the ξ_t phasor. The results are shown in Figure 4, where the red line shows the ξ_m phasor and the yellow-shaded region gives a geometrically derived region of uncertainty, generated by the uncertainties in tidal phase and amplitude of ξ_t and ξ_s . Whenever the yellow-shaded region of ξ_m uncertainty contains the origin of the axes, the ξ_m phase cannot be determined; however, we can still provide an upper bound on its amplitude.

The largest ξ_m occurs at R07, where the ξ_m amplitude reaches 0.64 (+0.13, -0.14) mm and it lags 15° (+7, -5) $^\circ$ behind ξ_s . The second largest ξ_m occurs at R10 with amplitude of 0.4 (+0.51, -0.22) mm, and it occurs 142° (+26, -100) $^\circ$ ahead of ξ_s . R04 has ξ_m amplitude of 0.23 (+0.12, -0.11) mm, and it is in phase (+21, -20) $^\circ$ with ξ_s . At Site5c the ξ_m amplitude is 0.19 (± 0.11) mm, and it lags 19° (+33, -12) $^\circ$ behind ξ_s . ξ_m is further detectable at R08 with 0.1 (+0.09, -0.07) mm amplitude and 46° (+74, -34) $^\circ$ lag behind ξ_s and at FSE1 with 0.06 (+0.04, -0.05) mm amplitude and 22° (+52, -21) $^\circ$ lag. At the remaining sites the uncertainty in ξ_m phase is sufficiently high to make it unclear whether the melt fluctuates tidally at these sites at all; however, upper bounds on ξ_m amplitude can still be calculated (graphically shown in Figure 4 and listed in Figure S3).

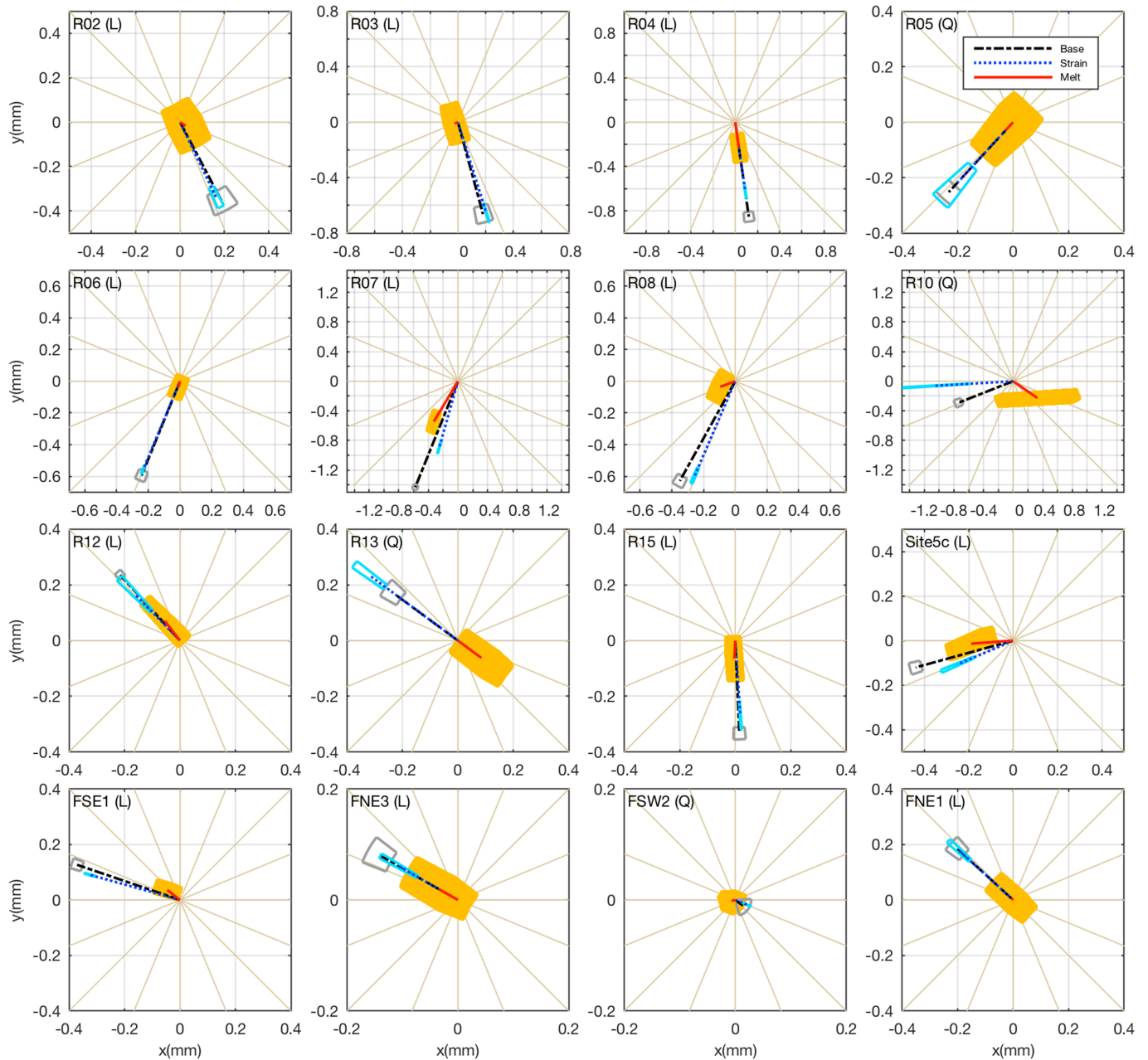


Figure 4. M_2 tidal basal reflector amplitude and phase partitioned into strain thinning and melt thinning contributions. Basal reflector is the black dashed line with gray box showing uncertainty. Strain thinning contribution is the dark blue dotted line with light blue box showing uncertainty. Melt thinning contribution is the red line with yellow region showing uncertainty. The plotted phase corresponds to the maximum displacement away from the radar antennas during the tidal cycle. The radial lines in the background are spaced by 22.5° . L and Q in parenthesis specify whether the linear or the quadratic fit was used for the estimate of the strain contribution. Note that while the axis limits are different on each panel, the grid spacing is 0.2 mm on all panels.

4.5. Tidal Melt Rate and Strain Rate Versus Long-Term Mean

To assess the significance of the tidal effects, we convert the ApRES-derived ξ_m and ξ_s to tidal melt rate and strain rate and compare it with the long-term mean rates. The tidal melt rate amplitude (units of m/year), M_R , is computed from the ξ_m amplitude, M , as $M_R = M2\pi f_{M_2}$, where f_{M_2} is the M_2 tidal frequency. The tidal strain rate amplitude (units of year⁻¹) is calculated analogously, but in addition, the ξ_s amplitude is divided by total ice thickness.

Figure 5a compares the long-term mean strain rate with the tidal strain rate amplitude for sites with depth-independent vertical strain rate. At most sites the tidal strain rate amplitude is larger than the

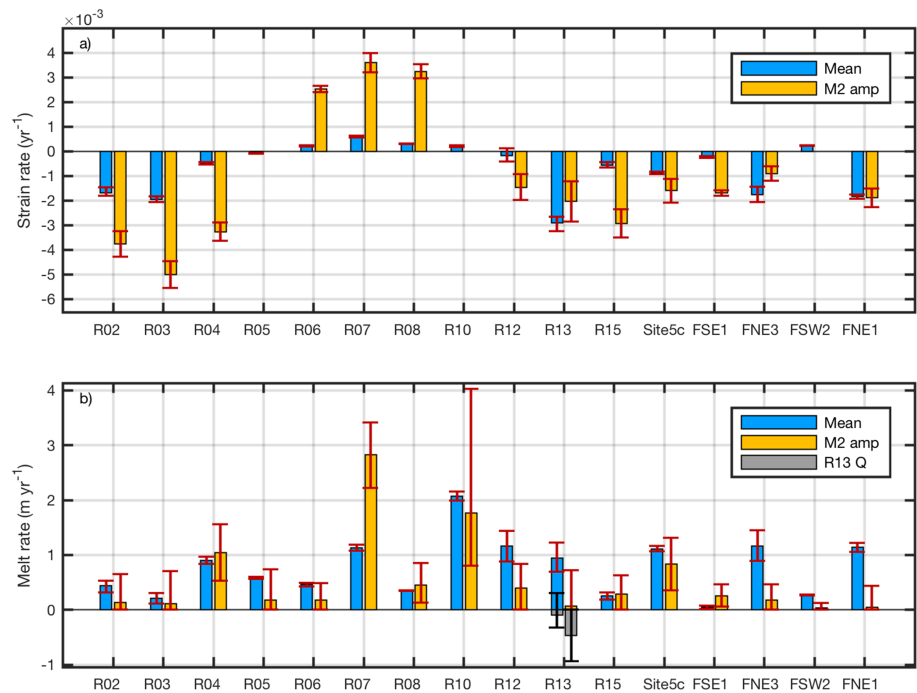


Figure 5. Comparison of long-term mean and tidal motion and basal melting. (a) The long-term mean strain rate and the amplitude of M_2 tidal vertical strain rate; sites with depth-dependent vertical strain rate are omitted. (b) Same as (a) but for melt rate. Results for R13 using a quadratic fit to the depth displacement profile are shown in gray. The sign of tidal melt/strain rate amplitude in the figure is chosen to be the same as that of the respective long-term mean.

long-term strain rate. One area where this does not occur is where the cluster of sites FNE3, FNE1, and R13 is located, closest to the Filchner Ice Shelf front. At these sites the tidal strain rate is almost as large as the long-term mean. Makinson et al. (2012) used surface velocity observations to show that the ice shelf regularly reverses its flow direction depending on the phase of the tidal cycle; these new ApRES data show that the tidal cycle also controls the sign of the ice shelf total horizontal divergence and, therefore, ice deformation.

Figure 5b compares the long-term mean melt rate with the tidal melt rate amplitude. All sites, with the possible exception of R13, are melting on average. There are six sites with tidal melt rate amplitude larger than its uncertainty, of which R04, R07, R10, and Site5c show a substantial tidal melt rate amplitude. At the remaining 10 sites the M_2 tidal melt rate is either absent or below our resolution limit; however, as further discussed in section 5, this does not necessarily imply that ocean tidal dynamics is weak at these locations.

5. Discussion

Variations in basal melt rate over a tidal cycle are affected by tidal fluctuations of water speed and temperature near the ice shelf base. If there is a horizontal gradient in temperature, it will be moved with the tidal flow, causing the native M_2 frequency to appear in the melt rate signal. The tidal flow itself can cause melt rate variations by affecting the heat diffusivity in the ocean boundary layer at the base of the ice shelf. This turbulent diffusivity is usually parameterized as a function of shear stress at the ice-ocean interface, which is often expressed in terms of free stream speed beyond the boundary layer. Therefore, in absence of horizontal temperature gradient, it is only the flow speed, and not the flow direction, that affects the magnitude of the heat transfer to the ice shelf.

The way the tidal flow variation is manifested in the melt rate depends on the characteristics of the tidal current ellipse, on the nontidal background flow, and on the relative orientation of the background flow and the tidal ellipse. These variables control the relative importance of tidal frequencies and their multiples in the melt rate. Figure 6a shows several synthetic examples of flow speed time series resulting from different values of these variables. If the background flow is relatively strong, we expect the native M_2 constituent to be the dominant frequency in speed, and therefore melt rate. If the flow speed is dominated by tides, the

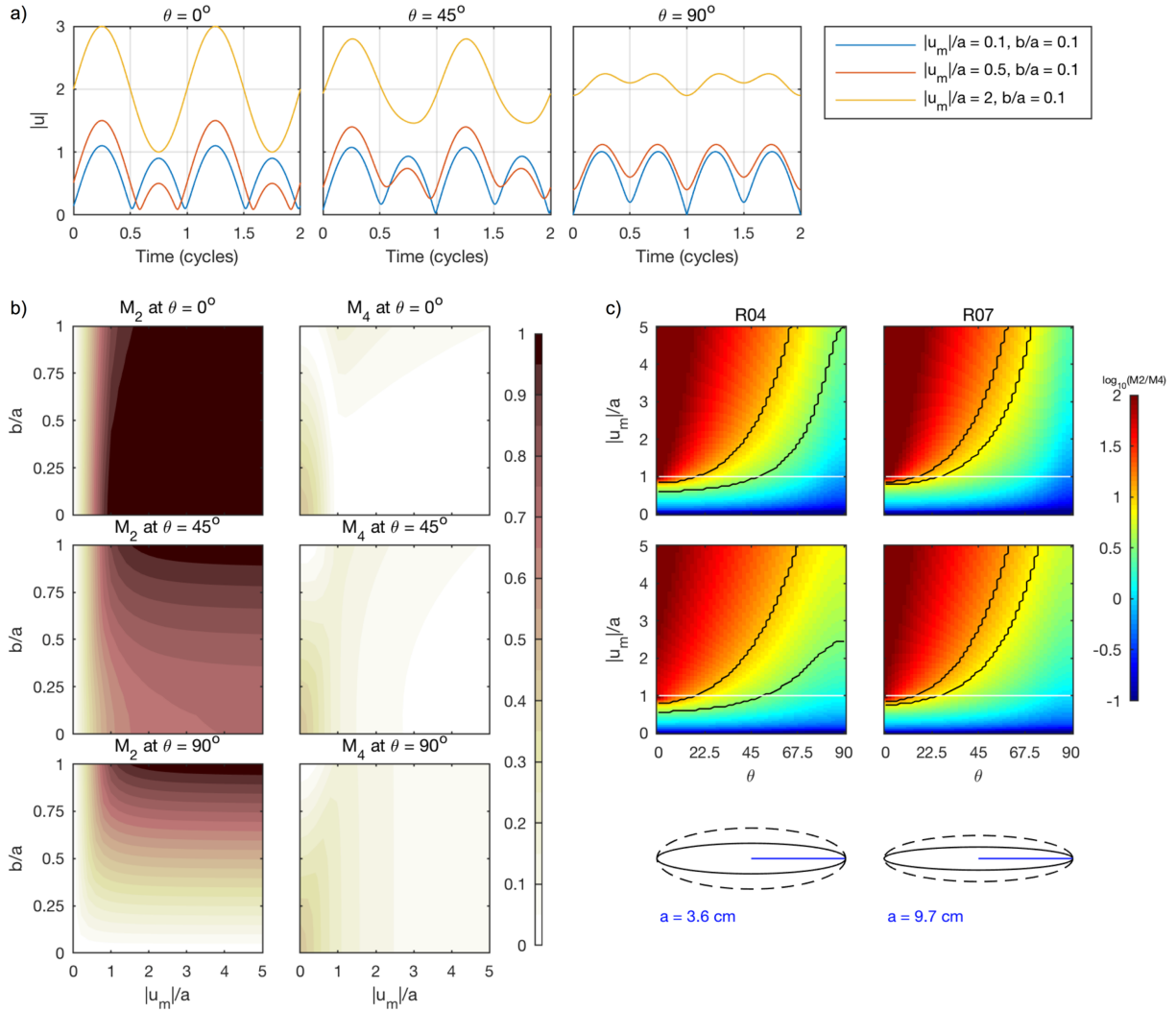


Figure 6. (a) Examples of flow speed for different combinations of three parameters: b/a , the ratio of semiminor axis b to semimajor axis a of a tidal ellipse; $|\vec{u}_m|/a$, the ratio of the background flow speed and the length of the tidal semimajor axis; and θ , the angle between the background flow and the semimajor axis. (b) Dependence of the strength of the M_2 and M_4 tidal frequency constituents in the total flow speed on the three parameters. (c) Permissible background flow regimes beneath the ice shelf at two observed sites. The colormap shows the ratio of the amplitude of the M_2 and M_4 tidal constituents in the total water speed for varying speed and directions in the background flow relative to the tidal ellipse. Black contour encloses the range of observed M_2 and M_4 tidal melt rate amplitude ratios within the uncertainty. Two different values of b/a are considered: In the first row we show results using the b/a value extracted from the barotropic tidal model at the nearest grid cell, and in the second row this value is doubled to show the sensitivity to the ellipse characteristics. The respective ellipses are shown as black solid and black dashed lines with their semimajor axis shown in blue and their length noted under the ellipses. The white line indicates where $|\vec{u}_m| = a$.

speed will have a significant double-frequency component, so we expect to find $2 \times M_2$ (M_4) in the melt rate spectrum. However, if the tidal ellipse is close to circular, there will be no tidal flow-induced tidal melt rate variability, unless there is a significant temperature gradient being advected.

This effect is now considered systematically. We assume that the time-dependent velocity near the ice base $\vec{u}(t) = (u(t), v(t))$ is the sum of a constant nontidal background flow $\vec{u}_m = (u_m, v_m)$ and a tidal flow oscillating at the f_{M_2} frequency:

$$\begin{aligned} u(t) &= u_m + u_T \sin(2\pi f_{M_2} t + \gamma_u) \\ v(t) &= v_m + v_T \sin(2\pi f_{M_2} t + \gamma_v), \end{aligned} \quad (2)$$

where u_T and v_T are amplitudes of each tidal vector component and γ_u and γ_v are the respective tidal phases. The frequencies present in the melt rate will then reflect the frequencies present in the speed $|\vec{u}(t)|$. This

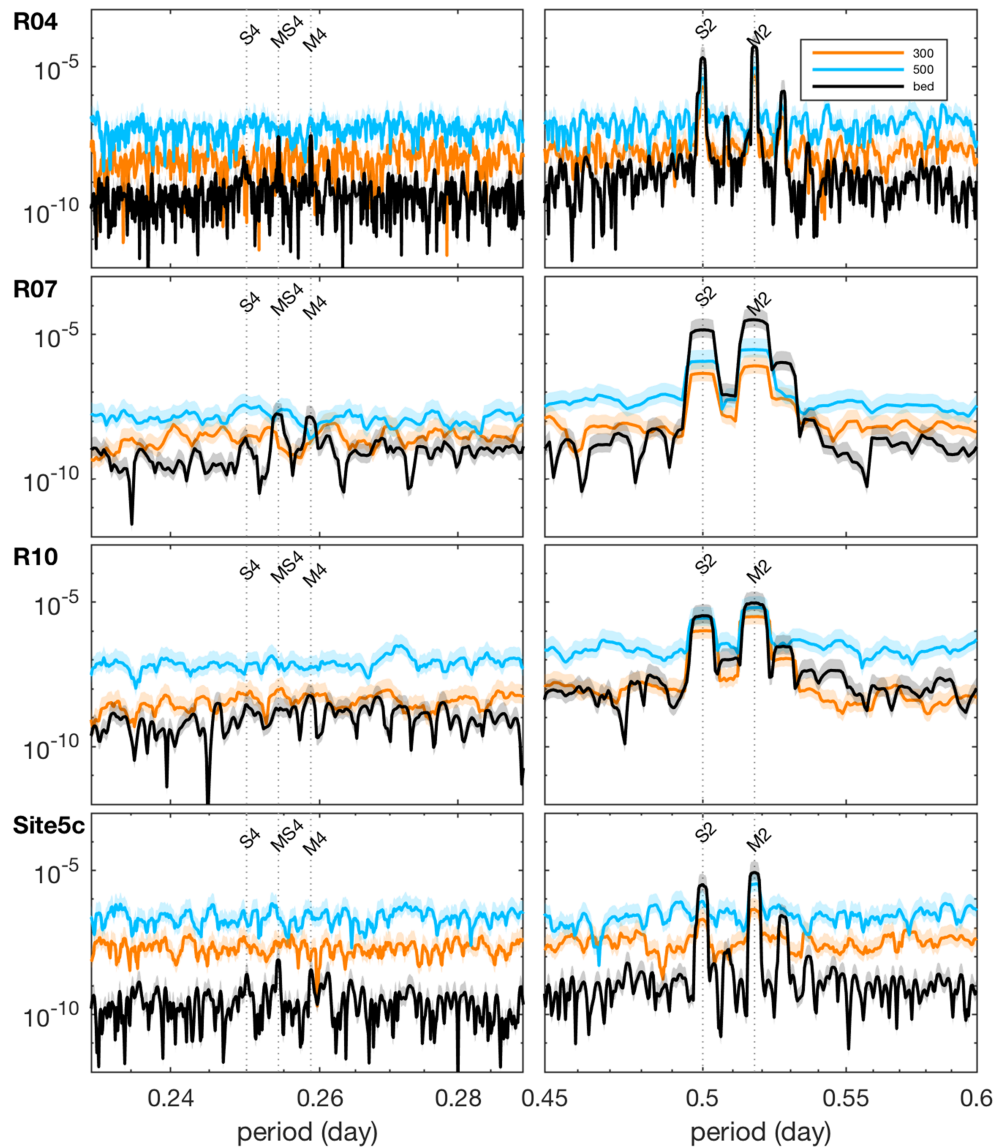


Figure 7. Power spectrum of the basal reflector time series and internal reflector time series at 300- and 500-m depth: black, orange, and blue lines, respectively, with 95% confidence level shaded.

setup can be reduced to three parameters: b/a , the ratio of semiminor axis b to semimajor axis a of a tidal ellipse; $|\bar{u}_m|/a$, the ratio of the background flow speed and the length of the tidal semimajor axis; and θ , the angle between the background flow and the semimajor axis.

Figure 6b shows how the relative contribution between M_2 and M_4 depends on these three parameters. For small background flow M_2 is absent or small compared with M_4 , except when the ellipse becomes close to circular and the tidal variation in flow speed is zero. The reason for the appearance of the M_4 double-frequency constituent is that the flow passes through its minimum and maximum twice in a tidal cycle. Further, for small background flows M_4 increases with decreasing b/a (increasing eccentricity) as the difference between the minimum and maximum tidal flow speed increases. For low b/a (high eccentricity) and as θ approaches 90° , the M_4 appears again for the same reason as above although with low amplitude (see, e.g., the third panel of Figure 6a). The relative proportion of M_2 increases as the background flow increases and as the tidal ellipse and background flow become aligned (low θ). An important implication of these results is that with a change in the background flow the relative M_2 and M_4 contributions in the melt rate will also change.

The importance of the background flow for the expression of a native tidal constituent and its double-frequency constituent in the melt rate suggests the following question: Can we infer properties of the background flow from the observed melt rate?

To address this, we turn back to the ApRES data and investigate the spectrum of the basal and internal reflector time series focusing on the semidiurnal and quarterdiurnal range. Figure 7 shows the relevant part of the spectrum for four sites where significant M_2 melt rate was detected (R04, R07, R10, and Site5c), but they are representative of other sites as well. Two example internal reflectors are shown, one located at 300-m depth and the other at 500-m depth. The two strongest peaks in the semidiurnal portion of the spectrum are M_2 and S_2 , both of which are present in the basal and internal reflector time series. For R04 and R07 there are quarterdiurnal tidal frequencies M_4 , MS_4 , and S_4 that stand out in the spectra of the basal reflector time series. However, these peaks do not appear in the internal reflector time series. This is either because this signal is not present in the ice shelf motion or because the noise level in the internal reflector time series is too high to allow them to be seen. Because the background noise in the internal reflectors is higher than the amplitude of the quarterdiurnal peaks in the basal reflector, we cannot be certain whether these peaks are caused by ice dynamics or by basal melt.

The M_4 , MS_4 , and S_4 frequencies arise from nonlinear interaction between M_2 and M_2 , M_2 and S_2 , and S_2 and S_2 native tidal constituents, respectively. One nonlinear mechanism that would explain the presence of the quarterdiurnal peaks in the basal reflector spectrum is the melt rate dependence on water speed near the ice shelf base (Figure 6b, right panel). On the other hand, it is possible that fluctuations at these quarterdiurnal constituents in either temperature or velocity are already present in the water column as a result of shallow water interactions. The double-frequency components may also be introduced from the ice dynamics. Rosier and Gudmundsson (2018) suggested a flexural softening mechanism that should give rise to these double frequencies at significant levels. However, Rosier and Gudmundsson (2019) concluded that this mechanism may not be important at FRIS.

To illustrate how high-frequency observations of melt rates could be used to constrain the regime of the flow beneath the ice shelf, we need to make the following three assumptions: (1) Horizontal temperature gradients are small, and tidal melt rate is effectively a function of flow speed only; (2) tidal melt rate is a linear function of flow speed, and the ocean velocity takes the form of equation (2); and (3) the M_4 tidal signal in the basal reflector time series is introduced from M_2 forcing via the melt rate dependence on water speed. Now, for a given tidal current ellipse eccentricity, we can use the ratio of tidal melt rate amplitude at the M_2 and M_4 frequencies to extract a range of possible background flow speeds at a range of possible angles θ .

Figure 6c shows this range of regimes for R04 and R07, which have both M_2 and M_4 constituents detected at significant levels. The M_2 tidal ellipse eccentricities of the barotropic flow are extracted from CATS2008 at the respective sites. The tidal melt rate amplitude at the M_2 constituent is stronger than at the M_4 constituent by an order of magnitude at both sites. This indicates either that the background flow is relatively strong or that the tidal melt rate contribution from the unknown and neglected horizontal temperature gradient is important. The same holds for the remaining ApRES sites where M_4 is a significant constituent in the basal reflector time series: M_4 in the basal reflector is much lower than our best estimate of ξ_m at the M_2 frequency. Consequently, we do not observe a regime of low nontidal background flow and high tidal current ellipse eccentricity. However, it is possible that this regime does occur, and if that is the case, it implies that horizontal temperature gradients are important for tidal melt rate variability.

6. Conclusions

We used ApRES to collect precise measurements of the evolution of an ice column and its base at 17 sites spread across Filchner-Ronne Ice Shelf. These measurements can be used to create time series of the vertical displacement of internal and basal reflectors. The quality of basal melt measurements relies on accurate estimation of the vertical strain in the ice. We have presented a method to estimate the vertical strain, and consequently the basal melt, fluctuations at tidal frequencies. The method was applied to all sites with focus on the predominant semidiurnal M_2 tidal constituent.

At 12 sites the tidal vertical strain was depth independent and consistent with a tilting ice shelf mechanism, known to explain well the FRIS semidiurnal tidal dynamics. At three sites, R05, R10, and FSW2, the tidal

vertical strain was found to be a linear function of depth, consistent with tidal bending. These sites were located near the grounding line, and although they experience tidal bending, the long-term mean vertical strain is depth independent. This indicates that while this portion of the ice shelf has adjusted to flotation in the viscous state, it is still sufficiently near the grounding line for tidal displacement from the equilibrium to result in elastic bending, rather than depth-independent deformation.

Upper bounds on M_2 tidal melt were derived at 16 sites, and significant tidal melt was detected at six sites. At two of those, R08 and FSE1, the tidal melt amplitude was small and its relative uncertainty large; also, the long-term mean melt rate at these sites was found to be small. However, at R04, R07, R10, and Site5c, which all experience a mean melt rate of $\sim 1\text{--}2$ m/year, the tidal melt rate was also high. The tidal melt rate was comparable with the long-term mean melt rate at R04 and Site5c, and at R07 it exceeded the long-term mean.

The causes of the tidal melt rate variations include tidal frequency fluctuations in temperature and water speed near the ice shelf base. Melt rate dependency on water speed introduces tidal shallow water constituents, such as M_4 , into the melt rate, and these are observed in the spectrum of the basal reflector time series at several sites. The proportion of M_2 and M_4 tidal amplitude in the observed melt rate spectrum were used to identify possible speeds and directions of the nontidal background flow beneath the ice shelf. The analysis omitted the unknown but potentially significant horizontal temperature gradients in the water column. If the horizontal temperature gradient is important, it will enhance the relative importance of the native M_2 tidal frequency and thus modify the range of possible nontidal background flows.

Here we have explored the limits of the ApRES observational technique and identified internal ice motion and basal melt down to semidiurnal tidal time scales, the fastest time scales that current deployments allow us to resolve, and which are believed to be detectable with this method. Basal melt spectra, and in particular the presence and relative importance of different tidal frequencies and their multiples, carry information about small-scale processes near the ice shelf base. ApRES observations, coupled with detailed measurements in the ice-ocean boundary layer, could enhance our understanding of processes controlling the basal melting of ice shelves around Antarctica.

Acknowledgments

This project has received funding from the European Union's Horizon 2020 research and innovation programme under the Marie Skłodowska-Curie Grant Agreement 790062. The ApRES data were collected as part of the NERC-funded project NE/L013770/1: Ice shelves in a warming world: Filchner Ice Shelf System (FISS), Antarctica. We thank Craig Stewart for sharing his code, Elin Darelus for her comments on an earlier version of the manuscript, and Laurie Padman, Olga Sergienko, and two anonymous reviewers for their detailed review which significantly improved the paper. The data set presented in this paper is available for download online (at <https://doi.org/10.6084/m9.figshare.10009010>).

References

- Brennan, P. V., Lok, L. B., Nicholls, K., & Corr, H. (2014). Phase-sensitive FMCW radar system for high-precision Antarctic ice shelf profile monitoring. *Sonar Navigation IET Radar*, 8(7), 776–786. <https://doi.org/10.1049/iet-rsn.2013.0053>
- Codiga, D. (2011). Unified tidal analysis and prediction using the UTide Matlab functions. <https://doi.org/10.13140/RG.2.1.3761.2008>
- Corr, H. F., Jenkins, A., Nicholls, K. W., & Doake, C. S. M. (2002). Precise measurement of changes in ice-shelf thickness by phase-sensitive radar to determine basal melt rates. *Geophysical Research Letters*, 29(8), 73–71. <https://doi.org/10.1029/2001GL014618>
- Davis, P. E. D., Jenkins, A., Nicholls, K. W., Brennan, P. V., Abrahamson, E. P., Heywood, K. J., et al. (2018). Variability in basal melting beneath Pine Island Ice Shelf on weekly to monthly timescales. *Journal of Geophysical Research: Oceans*, 123, 8655–8669. <https://doi.org/10.1029/2018JC014464>
- Doake, C. S. M. (1992). Gravimetric tidal measurements on Filchner Ronne Ice Shelf. *Filchner-Ronne Ice Shelf Programme Report*, 6, 34–39.
- Grosfeld, K., Blindow, N., & Thyssen, F. (1994). Bottom melting on the Filchner-Ronne Ice Shelf, Antarctica, using different measuring techniques. *Polarforschung*, 62(2-3), 71–76. <https://doi.org/10.2312/polarforschung.62.2-3.71>
- Gwyther, D. E., Cougnon, E. A., Galton-Fenzi, B. K., Roberts, J. L., Hunter, J. R., & Dinniman, M. S. (2016). Modelling the response of ice shelf basal melting to different ocean cavity environmental regimes. *Annals of Glaciology*, 57(73), 131–141. <https://doi.org/10.1017/aog.2016.31>
- Jenkins, A., Corr, H. F. J., Nicholls, K. W., Stewart, C. L., & Doake, C. S. M. (2006). Interactions between ice and ocean observed with phase-sensitive radar near an Antarctic ice-shelf grounding line. *Journal of Glaciology*, 52(178), 325–346. <https://doi.org/10.3189/172756506781828502>
- Makinson, K. (2002). Modeling tidal current profiles and vertical mixing beneath Filchner–Ronne Ice Shelf, Antarctica. *Journal of Physical Oceanography*, 32(1), 202–215. [https://doi.org/10.1175/1520-0485\(2002\)032<0202:MTCPAV>2.0.CO;2](https://doi.org/10.1175/1520-0485(2002)032<0202:MTCPAV>2.0.CO;2)
- Makinson, K., Holland, P. R., Jenkins, A., Nicholls, K. W., & Holland, D. M. (2011). Influence of tides on melting and freezing beneath Filchner-Ronne Ice Shelf, Antarctica. *Geophysical Research Letters*, 38, L06601. <https://doi.org/10.1029/2010GL046462>
- Makinson, K., King, M. A., Nicholls, K. W., & Gudmundsson, G. H. (2012). Diurnal and semidiurnal tide-induced lateral movement of Ronne Ice Shelf, Antarctica. *Geophysical Research Letters*, 39, L10501. <https://doi.org/10.1029/2012GL051636>
- Makinson, K., & Nicholls, K. W. (1999). Modeling tidal currents beneath Filchner-Ronne Ice Shelf and on the adjacent continental shelf: Their effect on mixing and transport. *Journal of Geophysical Research*, 104(C6), 13,449–13,465. <https://doi.org/10.1029/1999JC900008>
- Mueller, R. D., Hattermann, T., Howard, S. L., & Padman, L. (2018). Tidal influences on a future evolution of the Filchner–Ronne Ice Shelf cavity in the Weddell Sea, Antarctica. *The Cryosphere*, 12(2), 453–476. <https://doi.org/10.5194/tc-12-453-2018>
- Nicholls, K. W., Corr, H. F., Stewart, C. L., Lok, L. B., Brennan, P. V., & Vaughan, D. G. (2015). A ground-based radar for measuring vertical strain rates and time-varying basal melt rates in ice sheets and shelves. *Journal of Glaciology*, 61(230), 1079–1087. <https://doi.org/10.3189/2015JoG15J073>
- Nicholls, K. W., Makinson, K., & Johnson, M. R. (1997). New oceanographic data from beneath Ronne Ice Shelf, Antarctica. *Geophysical Research Letters*, 24(2), 167–170. <https://doi.org/10.1029/96GL03922>
- Padman, L., Fricker, H. A., Coleman, R., Howard, S., & Erofeeva, L. (2002). A new tide model for the Antarctic ice shelves and seas. *Annals of Glaciology*, 34, 247–254. <https://doi.org/10.3189/172756402781817752>

- Padman, L., Siegfried, M. R., & Fricker, H. A. (2018). Ocean tide influences on the Antarctic and Greenland Ice Sheets. *Reviews of Geophysics*, *56*, 142–184. <https://doi.org/10.1002/2016RG000546>
- Rosier, S. H. R., & Gudmundsson, G. H. (2018). Tidal bending of ice shelves as a mechanism for large-scale temporal variations in ice flow. *The Cryosphere*, *12*(5), 1699–1713. <https://doi.org/10.5194/tc-12-1699-2018>
- Rosier, S. H. R., & Gudmundsson, G. H. (2019). Exploring mechanisms responsible for tidal modulation in flow of the Filchner-Ronne Ice Shelf. *The Cryosphere Discussions*, 1–31. <https://doi.org/10.5194/tc-2019-79>
- Scheduik, M., & Olbers, D. J. (1990). A one-dimensional mixed layer model beneath the Ross Ice Shelf with tidally induced vertical mixing. *Antarctic Science*, *2*(1), 29–42. <https://doi.org/10.1017/S0954102090000049>
- Stewart, C. L. (2018). Ice-ocean interactions beneath the north-western Ross Ice Shelf, Antarctica, Thesis, University of Cambridge. <https://doi.org/10.17863/CAM.21483>
- Stewart, C. L., Christoffersen, P., Nicholls, K. W., Williams, M. J. M., & Dowdeswell, J. A. (2019). Basal melting of Ross Ice Shelf from solar heat absorption in an ice-front polynya. *Nature Geoscience*, *12*(6), 435. <https://doi.org/10.1038/s41561-019-0356-0>
- Vaňková, I., Voytenko, D., Nicholls, K. W., Xie, S., Parizek, B. R., & Holland, D. M. (2018). Vertical structure of diurnal englacial hydrology cycle at Helheim Glacier, East Greenland. *Geophysical Research Letters*, *45*, 8352–8362. <https://doi.org/10.1029/2018GL077869>
- Vaughan, D. G., Corr, H. F. J., Bindschadler, R. A., Dutrieux, P., Gudmundsson, G. H., Jenkins, A., et al. (2012). Subglacial melt channels and fracture in the floating part of Pine Island Glacier, Antarctica. *Journal of Geophysical Research*, *117*, F03012. <https://doi.org/10.1029/2012JF002360>